Science of the Total Environment 718 (2020) 137294

Contents lists available at ScienceDirect

Science of the Total Environment

journal homepage: www.elsevier.com/locate/scitotenv

# Role of biogenic Fe(III) minerals as a sink and carrier of heavy metals in the Rio Tinto, Spain

Sergey M. Abramov [a,b,*], Julian Tejada [c], Lars Grimm [a], Franziska Schädler [a,b], Aleksandr Bulaev [d], Elizabeth J. Tomaszewski [a,e], James M. Byrne [a], Daniel Straub [b], Harald Thorwarth [c], Ricardo Amils [f], Sara Kleindienst [b], Andreas Kappler [a]

[a] Geomicrobiology, Center for Applied Geosciences, University of Tuebingen, Hölderlinstrasse 12, D-72074 Tuebingen, Germany
[b] Microbial Ecology, Center for Applied Geosciences, University of Tuebingen, Hölderlinstrasse 12, D-72074 Tuebingen, Germany
[c] University of Applied Forest Sciences Rottenburg, Schadenweilerhof, D-72108 Rottenburg am Neckar, Germany
[d] Winogradsky Institute of Microbiology, Research Center of Biotechnology of the Russian Academy of Sciences, Leninsky Ave. 33, Bld 2, 119071 Moscow, Russia
[e] Plant and Soil Sciences 250A Harker ISE Lab, University of Delaware Newark, DE 19716, USA
[f] Department of Virology and Microbiology, Centre for Molecular Biology "Severo Ochoa", Autonomous University of Madrid, Calle Nicolás Cabrera 1, Cantoblanco (Campus UAM), 28049 Madrid, Spain

## HIGHLIGHTS

- Acidophilic Fe(II) oxidizers form cell-Fe (III) mineral aggregates consisting of schwertmannite and ferrihydrite.
- Sedimentation of suspended particulate matter lead to burial of heavy metals in the river and estuarine sediment.
- Up to 100% of As and Cr can be transported to the estuary of the Rio Tinto by suspended particulate matter.

## GRAPHICAL ABSTRACT

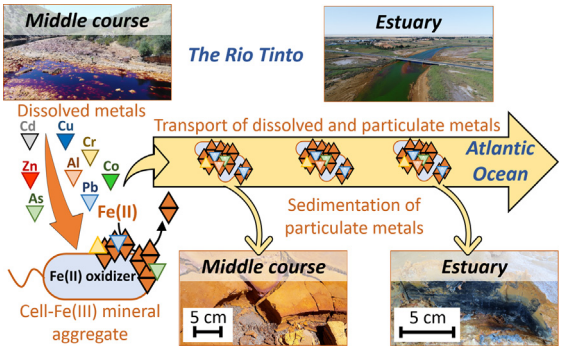


## ARTICLE INFO

*Article history:*
Received 19 December 2019
Received in revised form 11 February 2020
Accepted 11 February 2020
Available online xxxx

Editor: Filip M.G. Tack

*Keywords:*
Rio Tinto
Heavy metal
Microbial Fe(II) oxidation
Suspended particulate matter
Contaminated river

## ABSTRACT

Oxidation of sulfide ores in the Iberian Pyrite Belt region leads to the presence of extremely high concentration of dissolved heavy metals (HMs) in the acidic water of the Rio Tinto. Fe(II) is microbially oxidized resulting in the formation of suspended particulate matter (SPM) consisting of microbial cells and Fe(III) minerals with co-precipitated HMs. Although substantial amount of HM-bearing SPM is likely deposited to river sediment, a portion can still be transported through estuary to the coastal ocean. Therefore, the mechanisms of SPM formation and transport along the Rio Tinto are important for coastal-estuarine zone. In order to reveal these mechanisms, we performed diurnal sampling of Rio Tinto water, mineralogical and elemental analysis of sediment from the middle course and the estuary of the river. We identified two divergent but interrelated pathways of HM transfer. The first longitudinal pathway is the transport of SPM-associated metals such as As (6.58 μg/L), Pb (3.51 μg/L) and Cr (1.30 μg/L) to the coastal ocean. The second sedimentation pathway contributes to the continuous burial of HMs in the sediment throughout the river. In the middle course, sediment undergoes mineralogical transformations during early diagenesis and traps HMs (e.g. 1.6 mg/g of As, 1.23 mg/g of Pb and 0.1 mg/g of Cr). In the estuary, HMs are accumulated in a distinct anoxic layer of sediment (e.g. 1.5 mg/g of As, 2.09 mg/g of Pb and

* Corresponding author at: Geomicrobiology, Center for Applied Geosciences, University of Tuebingen, Hölderlinstrasse 12, D-72074 Tuebingen, Germany.
*E-mail address:* sergey.abramov@uni-tuebingen.de (S.M. Abramov).

https://doi.org/10.1016/j.scitotenv.2020.137294

Estuary

0.04 mg/g of Cr). Our results indicate that microbially precipitated Fe(III) minerals (identified as ferrihydrite and schwertmannite) play a key role in maintaining these divergent HM pathways and as a consequence are crucial for HM mobility in the Rio Tinto.



## 1. Introduction

The Rio Tinto in the province of Huelva, Spain, is of great interest as it is one of the most heavy metal (HM) contaminated fluvial-estuarine systems in the world (Amils et al., 2007). This is largely due to the underlying geology of the area, as the Rio Tinto flows through the mining region of the Iberian Pyrite Belt (Olías and Nieto, 2015). Open-pit mines, waste-rock piles and tailings as well as naturally exposed outcrops of sulfides located along the northern zone of the river are subject to high levels of weathering, partly controlled by microorganisms (Fernández-Remolar et al., 2003). Microbial oxidation of sulfide ores leads to release of HMs (e.g. Fe, Al, Zn, Cu, Cd, Cr, As, Pb and Co) into the Rio Tinto. Part of the HM load is deposited in river and estuarine sediments. However, a significant portion of HMs eventually enters the coastal ocean (Elbaz-Poulichet et al., 2000; Fernández-Remolar et al., 2003; Periáñez, 2013). For example dissolved Zn and Cu transported by the Rio Tinto to the ocean constitute from 0.69% to 9.4% and from 0.3% to 3.7% of the global gross river fluxes of these metals, respectively (Braungardt et al., 2003; Nieto et al., 2007; Nieto et al., 2013).

In addition to aqueous species, the river can also transport HMs as solids, such as those that are associated with suspended particulate matter (SPM; Cánovas et al., 2012a; Mosley and Liss, 2019). The formation of SPM is caused by the unique Fe-based hydro(bio)geochemistry of the river (España et al., 2005; Sánchez España et al., 2006). Ongoing microbial oxidation of dissolved Fe(II) in the water column leads to a pH increase due to consumption of $H^+$ according to Eq. (1) (Campaner et al., 2014; Siew et al., 2020). However, following precipitation of Fe(III) (oxyhydr)oxides (Eq. (2)) or hydroxysulphates (Eq. (3)), the $H^+$ pool in the river water is replenished and the pH is kept low (Dold, 2014; Song et al., 2018; Siew et al., 2020). Precipitated Fe(III) minerals with co-precipitated HMs can remain suspended in the water column and eventually enter the coastal ocean (Cánovas et al., 2012a).

$$4Fe^{2+} + O_2 + 4H^+ \rightarrow 4Fe^{3+} + 2H_2O \quad (1)$$

$$4Fe^{3+} + 7H_2O \rightarrow 2Fe_2O_3 \times 0.5(H_2O) + 12H^+ \quad (2)$$

$$16Fe^{3+} + 2SO_4{}^{2-} + 28H_2O \rightarrow Fe_{16}O_{16}(OH)_{12}(SO_4)_2 + 44H^+ \quad (3)$$

Although some of the transported HMs such as Fe, Mn, Cu, Ni and Zn are essential biological micronutrients and required for growth of many aquatic organisms at high concentrations they can also become toxic (Zhang et al., 2018). Other metals, such as As, Cr, Pb and Cd, are not necessary for growth and even trace amounts of these can be toxic to marine organisms (Neff, 2002; Yilmaz et al., 2018). Therefore, the mechanisms of SPM formation in the water column of the Rio Tinto and subsequent transport of SPM along the Rio Tinto are important for ecology of coastal-estuarine zone (Elbaz-Poulichet et al., 2001; Achterberg et al., 2003; Braungardt et al., 2003; Cánovas et al., 2012b; Mosley and Liss, 2019).

Consequently, the aim of this work was to evaluate the impact of Fe (II)-oxidizing microorganisms on SPM formation and HM transport along the Rio Tinto. Detailed water sampling in the middle course and in the estuary in June/July 2017 and the analysis of in vivo processes of microbially supported SPM formation in the presence of HMs allowed for a better understanding of the fate of HMs in the Rio Tinto system.

## 2. Materials and methods

### 2.1. Field sites and sampling procedure

The Rio Tinto basin is divided into two main zones based on topological, geological and geochemical characteristics: the northern zone (consisting of headwaters and the middle course of the river) and the estuary. The northern zone is characterized by acidic pH (mean value 2.3). The estuary is located along a mesotidal coast, with a mean tidal range of 2.1 m and a daily pH gradient of 2.1–6.9 (Davis et al., 2000; Borrego et al., 2002; de la Torre et al., 2010; Hierro et al., 2014).

Samples were collected from 29.06.2017 to 02.07.2017 during the dry season with low flow rate in the middle course of the Rio Tinto near Berrocal village (field site 1; 37°35′36.0″N 6°33′04.5″W) and in the estuary under the bridge in San Juan del Puerto (field site 2; Fig. 1a–c; 37°18′40.3″N 6°49′22.4″W). River water was sampled in triplicate every 2 h for two days (29.06.2017–31.06.2017) at field site 1 and for one day (01.07.2017–02.07.2017) at field site 2. During the sampling event directly in the field, 2 L of water at field site 1 and 1 L at field site 2 were pre-filtered with 8 μm pore-size membrane filters (SCWP04700; Merck) to collect coarse-grained particles and then filtered with 0.45 μm pore-size membrane filter (HAWG050S6; Merck) for collection of fine-grained particles. Filters were subsequently placed in 2 mL centrifuge tubes and kept dark and at room temperature for further analysis. Filtered water was collected, stabilized and stored for the HM and anion analysis as described in the Appendix A (Section 1.1). Sediment samples were collected from the bank of the river at both field sites as described in the Appendix A (Section 1.2). The temperature, $E_h$, pH, salinity, and oxygen saturation of the water were determined in situ at both sites as described in the Appendix A (Section 1.3).

### 2.2. Cultivation of a Fe(II)-oxidizing microbial consortium

In this study, an acidophilic chemolithoautotrophic Fe(II)-oxidizing microbial consortium was established aerobically using river water from field site 1 in a modified basal salts/trace elements medium (Ňancucheo et al., 2016) supplemented with a Fe(II) sulfate. Basal salt solution consisted of 0.15 g/L $Na_2SO_4 \times 10H_2O$, 0.45 g/L $(NH_4)_2SO_4$, 0.5 g/L KCl, 0.5 g/L $MgSO_4 \times 7H_2O$, 0.5 g/L $KH_2PO_4$, and 0.014 g/L $Ca(NO_3)_2 \times 4H_2O$. The volume of the medium was adjusted up to 1 L with MQ-$H_2O$. The pH of the medium was adjusted with 10% $H_2SO_4$ to the in situ pH (i.e. pH 2.3). The medium was transferred into 1 L glass bottles, heat-sterilized (120 °C for 20 min), and supplemented with 1 mL of stock solution of trace elements consisting of 10 g/L $ZnSO_4 \times 7H_2O$, 1 g/L $CuSO_4 \times 5H_2O$, 1 g/L $MnSO_4 \times 4H_2O$, 1 g/L $CoSO_4 \times 7H_2O$, 0.5 g/L $Cr_2(SO_4)_3 \times 15H_2O$, 0.6 g/L $H_3BO_3$, 0.5 g/L $Na_2MoO_4 \times 2H_2O$, 1 g/L $NiSO_4 \times 6H_2O$, 1 g/L $Na_2SeO_4 \times 10H_2O$, 0.1 g/L $Na_2WO_4 \times 2H_2O$, 0.1 g/L $NaVO_3$. Then, the medium was transferred into a conical flask and supplemented with 1 M filter-sterilized $FeSO_4 \times 7H_2O$ solution to the final concentration 2.5 g/L. Cultivation was carried out in triplicate on a shaker at 150 rpm at 26 °C in the dark. Cultivation medium was sampled daily for one or two week for determination of cell numbers, pH, total Fe, Fe(II) and visual observations by light microscopy. Cells harvested at the exponential growth phase were used for quantification of Fe(II) oxidation rates as described in the Appendix A (Section 1.4).

Cultivation of a Fe(II)-oxidizing consortium under high HM load was carried out in basal salt medium supplemented with 12.7 g/L $Al_2(SO_4)_3$,

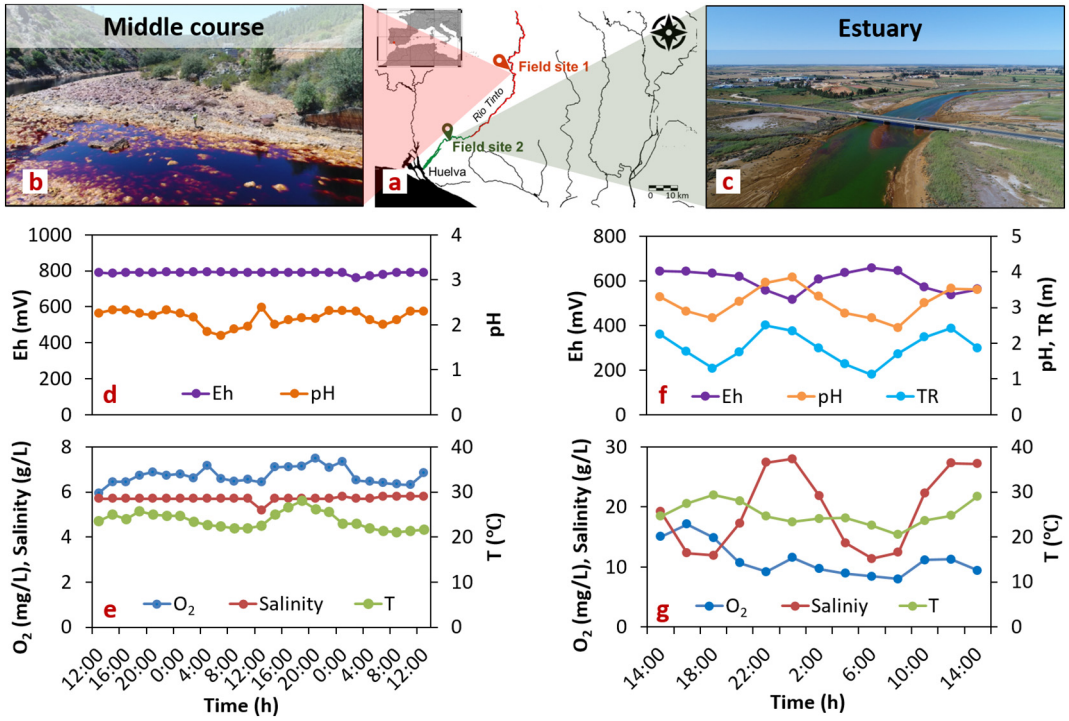


**Fig. 1.** Location and main hydro(bio)geochemical characteristics of the water at field site 1 (middle course) and field site 2 (estuary) of the Rio Tinto (June/July 2017). a, b, c. Location map and general view showing the middle course and estuary along the Rio Tinto. d, e. Diurnal dynamics of Eh, pH, $O_2$ content, salinity and temperature (T) of the river water at field site 1 (sampled 29.06.2017–31.06.2017). f, g. Tidal range (TR) fluctuation and diurnal dynamics of Eh, pH, $O_2$ content, salinity and T of the estuarine water at field site 2 (sampled 01.07.2017–02.07.2017).

625 mg/L $ZnCl_2$, 730 mg/L $CuSO_4 \times H_2O$, 50 mg/L$CoNO_3 \times 6H_2O$, 3 mg/L $NaAsO_2$, 2.8 mg/L $Pb(NO_3)_2$, 3.9 mg/L $Cd(NO_3)_2 \times 4H_2O$ and 3.1 mg/L $CrCl_3$. Experiments were carried out in triplicate, in the dark at 26 °C. Cultivation medium was sampled daily for determination of cell number, total Fe, Fe(II), HMs and for light and electron microscopy.

### 2.3. DNA extraction and 16S rRNA gene amplicon sequencing

For collection of free-living and particle-associated cells, we filtered 2 L of river water through 8 μm (SCWP04700; Merck) and 0.22 μm (GSWG047S6; Merck) pore size mixed cellulose ester (MCE) filters on site. Cells from the enriched microbial consortium were collected by filtration of cultivation medium through 0.22 μm pore size MCE filters (GSWG047S6; Merck). All filters were placed in sterile 2 mL centrifuge tubes and stored at −20 °C for further analysis. Total DNA was extracted according to Lueders et al. (2004). Microbial 16S rRNA genes were amplified using primers 515F and 806R targeting the V4 region (Caporaso et al., 2010). Subsequent library preparation steps (Nextera, Illumina) and 250 bp paired-end sequencing with MiSeq (Illumina, San Diego, CA, USA) using v2 chemistry were performed by Microsynth AG (Switzerland) and between 50,000 and 210,000 read pairs were obtained for each sample. Sequence analysis, phylogenetic analysis and statistical analysis was performed as described in the Appendix A (Section 1.5).

### 2.4. Quantification of cell number

To quantify cell number, 200 μL of the microbial culture were transferred into 2 mL centrifuge tube and mixed with 600 μL of oxalate solution (28 g/L ammonium oxalate and 15 g/L oxalic acid, pH 3). The centrifuge tube was incubated for 4 min at room temperature shaken periodically, mixed with 1200 μL of 22 mM bicarbonate buffer (pH 7) and centrifuged with maximum speed (16,873 ×g) for 5 min. The supernatant was discarded, and the cell-containing pellet was resuspended in 800 μL of 22 mM bicarbonate buffer (pH 7), mixed with 0.8 μL of BacLight dye (ThermoFisher, USA), vortexed and incubated for 15 min in the dark, shaken periodically. This cell suspension (600 μL) was then transferred into three wells of a 96-well plate (200 μL each) and the cell number in each well was quantified with a flow cytometer (Attune NxT, ThermoFisher, USA).

### 2.5. Light and electron microscopy

For fluorescence microscopy, samples were stained with SYTO 9 stain (BacLight, Invitrogen, Carlsbad, CA) before analysis with a Leica DM 5500 B microscope (Leica Microsystems, Germany). For scanning electron microscopy (SEM), cell-Fe(III) mineral aggregates from the Fe (II)-oxidizing culture or SPM from the river were fixed in 2.5% glutaraldehyde and stored in a cold room overnight. The next day, samples were prepared on poly-L-lysine (TED PELLA, INC.) glass slides and then taken through a dehydration series consisting of 30, 70, 95 and 100% ethanol and two final steps with hexamethyldisilazane before samples were allowed to air dry. Finally, all samples were placed on aluminum stubs with carbon tape and sputter-coated with platinum (6–8 nm, SCD005, BAL-TEC, Liechtenstein, 35 mm working distance, 30 mA, 60 s). SEM micrographs were recorded with a secondary electron detector of a Leo Model 1450VP SEM (Carl Zeiss SMT AG, Germany).

### 2.6. Elemental analysis of liquid samples

The concentration of HMs in the cultivation medium of Fe(II)-oxidizing microorganisms, in the river and estuarine water (filtered with a 0.45 μm pore size syringe filter and stabilized with $HNO_3$) was analyzed with inductively coupled plasma - optical emission spectrometry (ICP-OES; SPECTROBLUE TI, Ametek). Dissolved Fe(II) and total Fe in the microbial cultures were quantified by the ferrozine assay using spectrophotometric plate reader (FlashScan 550; Analytic, Jena, Germany; Stookey, 1970). For calculation of Fe(III), the concentration of Fe(II) was subtracted from the total Fe concentration. Dissolved anions ($Cl^-$,

$PO_4^{3-}$ and $SO_4^{2-}$) in the water samples were quantified using a Dionex DX-120 Ion Chromatograph (Thermo, USA).

### 2.7. Elemental analysis of SPM and sediment samples

Closed microwave digestion was performed in a microwave system (Anton Paar Ltd. mod. multiwave GO Microwave digestion system). For analysis, each membrane filter or 0.125 g of powdered sediment were placed into a PTFE-TFM-digestion vessel. To each digestion vessel, 7.5 mL 37% HCl and 2.5 mL 65% $HNO_3$ were added. Two blank vessels without samples but with equal volumes of HCl and $HNO_3$ were also prepared for each digesting run. The following temperature gradient parameters were applied: step 1 (ramping for 20 min to max. 175 °C; 8.75 °C/min), step 2 (hold for 30 min at 175 °C), step 3 (ventilation for 20 min to 50 °C). After digestion, samples were adjusted to 50 mL with MQ-$H_2O$ and stored in the dark prior to analysis.

The content of HMs in the digests of SPM and sediment samples was analyzed with ICP-OES (SPECTROBLUE TI, Ametek). In addition, the elemental composition of sediment samples was determined by X-ray fluorescence (Bruker AXS S4 Pioneer XRF device, equipped with a 4 kW Rh-tube).

### 2.8. Mineralogical analysis of solid samples

For quantification of Fe minerals, the dried SPM, cell-Fe(III) mineral aggregates and sediment samples were diluted with polyvinylpyrrolidone (ratio 2 to 1, respectively) and pressed into 7-mm pellets using a KBr pellet press (International Crystal). All pellets were sealed in Kapton tape during analysis. X-ray absorption spectroscopy was performed at the Advanced Photon Source (APS) Materials Research Collaborative Access Team (MRCAT) beamline 10-BM-B and beamline 10-ID-B at Argonne National Laboratory. Beamline 10-BM-B employs a bend magnet source and a Si(111) monochromator and beamline 10-ID-B employs an undulator source and a Si(111) monochromator. Spectra were collected at the Fe K-edge (7.11 keV) in the range of $k = 0–12$ Å$^{-1}$. Data reduction, normalization and calibration were performed using the ATHENA program in the Demter software package (Ravel and Newville, 2005). Spectra were calibrated to a Fe reference foil spectrum collected during measurements. Principal component analysis (PCA) was used to estimate an appropriate number of standards needed to fit the spectra of the samples (Fig. A.1). Linear combination fitting (LCF) of $k^3$ weights Fe extended X-ray absorption fine structure (EXAFS) spectra was performed from $k = 2–12$ Å$^{-1}$ using standards collected at beamline 10-ID-B. This type of fitting offers a semi-quantitative approach to describe the composition of the Fe phases in the samples. SIXpack and ATHENA were used to perform PCA and LCF analysis (Ravel and Newville, 2005; Webb, 2005). Reference spectra used in fitting included goethite, ferrihydrite, hematite, pyrite, and schwertmannite. The reduced chi-squared from each fit as well as the error associated with each phase used during fitting can be found in Table A.1.

## 3. Results and discussion

### 3.1. Hydro(bio)geochemical characteristics of the middle course and estuary of the Rio Tinto

Mean values of pH and $E_h$ at field site 1 were 2.1 and 787.7 mV, respectively. Sulfate concentration was 4.3 g/L while the salinity was 5.7 g/L (Table A.2). We observed minor diurnal fluctuations of pH, temperature and $O_2$ content caused by day/night cycles (Fig. 1d, e). The sunlight led to the activation of photosynthetic activity and $O_2$ accumulation followed by microbial aerobic Fe(II) oxidation resulting in $H^+$ consumption (Eq. (1)). These processes could be responsible for the pH increase during the daylight hours. At field site 2, we observed clear fluctuations of hydro(bio)geochemical parameters, caused by seawater inflow (Fig. 1f, g). The mean pH value was 3.2 and ranged from 2.4 to 3.8 during 6 h, meaning that the upper estuarine environment was still acidic despite the mixing events with seawater, which led to an almost 3-fold increase in salinity (19.4 g/L with fluctuations in the range from 11.4 to 28.0 g/L). Considering the low concentrations of Na and Cl at field site 1 (below 40 mg/L and 150 mg/L, respectively) and the high concentration in seawater (10.8 and 19.4 g/L, respectively; Altaee et al., 2018), both elements can be used as an indicator of river water dilution. Based on this, seawater was calculated to account for 83% and 34% of estuarine water at high and low tide, respectively. Inflow of seawater contributed to the increase of mean pH and decrease of mean $E_h$ (601.6 mV; fluctuations from 515 to 657 mV during 6 h). Sulfate was replenished by both sea and river water; therefore, it fluctuated only in the range from 2.3–3.2 g/L (mean of 2.7 g/L). Temperature and $O_2$ increased during daylight hours and decreased during the night. However, tidal cycles also had an impact on the water geochemistry. Thus, the high tide correlating with a decrease in water temperature and an increase in $O_2$ even at night (Fig. 1f, g). The tidal range (ca. 1.5 m) also contributed to the formation of floodplain areas where the precipitation of evaporites was observed.

### 3.2. Concentration of heavy metals in the dissolved and SPM-associated fractions

The river water in the middle course was characterized by the lack of serious fluctuations in the concentrations of dissolved and SPM-associated Fe, Al, Zn, Cu, Cd, Cr, As, Pb and Co (Fig. 2a). Two days of water sampling in the middle course allowed us to calculate mean concentration values of HMs for both fractions (Table 1). Obtained results demonstrate that dissolved Fe (2003.3 mg/L), Al (718.5 mg/L), Zn (279.2 mg/L) and Cu (149.7 mg/L) prevailed in the acidic water while dissolved Cd (0.99 mg/L), Cr (0.003 mg/L), As (1.43 mg/L), Pb (0.04 mg/L) and Co (5.02 mg/L) were identified in trace quantities. Fine-grained and coarse-grained SPM (0.45–8 μm and >8 μm, respectively) sampled from the water in the middle course were predominantly associated with solid phase Fe (2.1 mg/L), Al (2.4 mg/L), Zn (0.125 mg/L) and Cu (0.067 mg/L). SPM-associated Cd (0.59 μg/L), Cr (0.65 μg/L), As (3.41 μg/L), Pb (8.7 μg/L) and Co (2.49 μg/L) were determined in trace concentrations (Table 1).

The mean concentration values of HMs listed in Table 1 were used for calculation the percentage of metal distribution between fine-grained and coarse-grained SPM. The fine-grained SPM contained higher quantities of Al (91.24%), Zn (66.56%), Cu (69.58%), Cd (73.00%), Cr (75.47%) and Co (68.52%) while As (71.39%) prevailed in the coarse-grained particles. Iron (51.31%) and Pb (56.96%) were almost equally distributed between both grain size fractions of SPM. Using an identical approach, we calculated percentage of metal distribution between dissolved and SPM-associated fractions (Table 1). Obtained results suggest that in the upper, highly acidic part of the river, the main fractions of Fe (99.92%), Al (99.67%), Zn (99.96%), Cu (99.95%), Cd (99.94%), As (99.76%) and Co (99.95%) were dissolved in the water. Consequently, ca. 20.51% and 17.38% of the amount of Cr and Pb were associated with SPM.

In the estuary, we observed a clear correlation of the concentrations of dissolved Fe, Al, Zn, Cu, Co, Cd and Pb as well SPM-associated Zn and Co with the tidal cycles (Fig. 2b). The content of these metals in the water increased during low tide and then decreased during high tide. The mixing with seawater in the estuary led to consistent diminution of dissolved Fe (from 2003.3 to 11.2 mg/L), Al (from 718.5 to 32.4 mg/L), Zn (from 279.2 to 7.2 mg/L), Cu (from 149.70 to 5.04 mg/L), Cd (from 0.99 to 0.03 mg/L), Cr (from 0.003 mg/L to below detection limit; 0.5 μg/L), As (from 1.43 to below detection limit; 5 μg/L) and Co (from 5.02 to 0.12 mg/L; Tables 1 and 2). An opposite pattern was observed for dissolved Pb; the mean concentration (0.06 mg/L; Table 2) was slightly higher in the estuarine water than in the water of the middle course (0.04 mg/L; Table 1). This pattern can be explained by release of Pb from Pb sulfates (e.g. anglesite) under

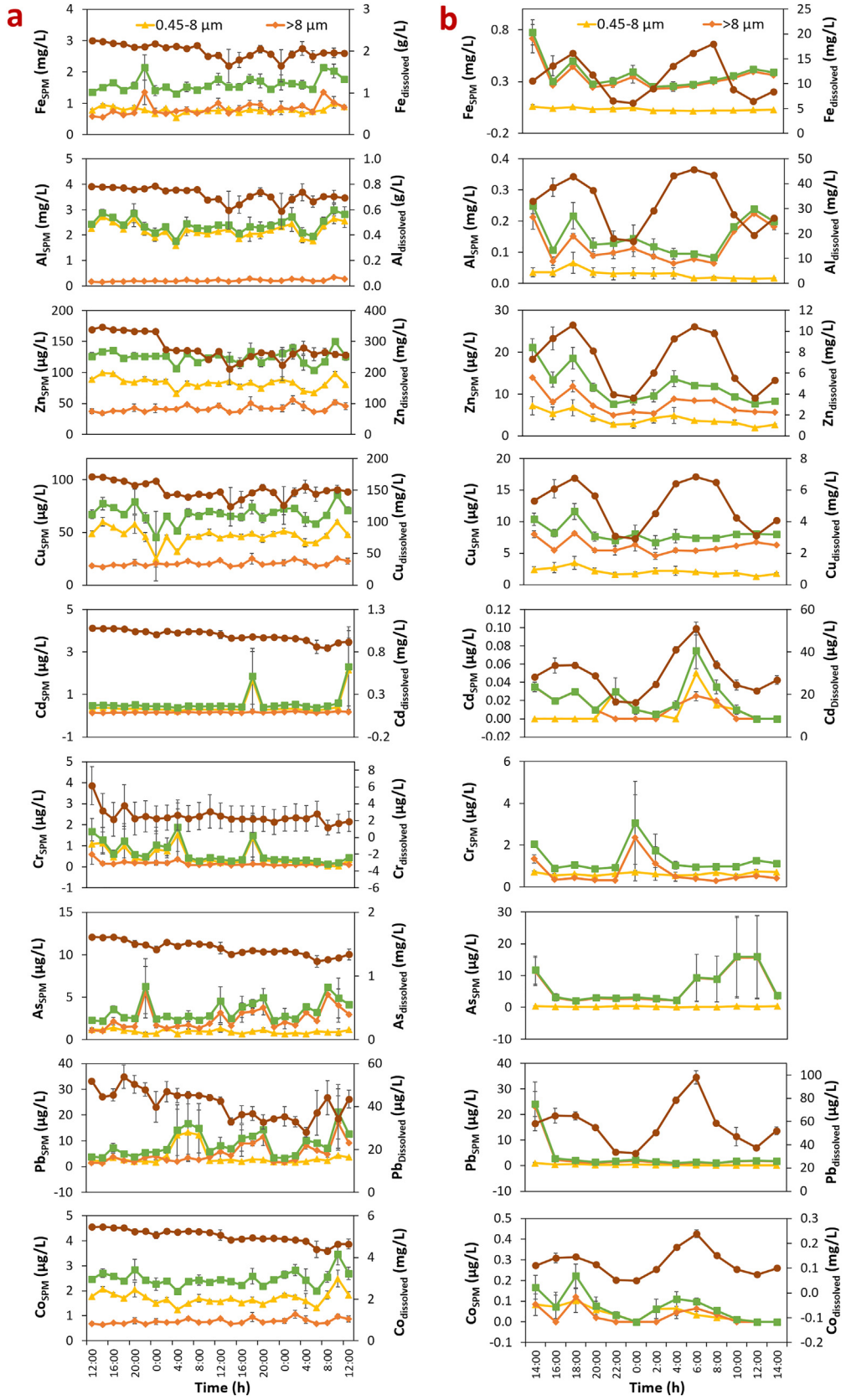


**Fig. 2.** Diurnal dynamics of dissolved and suspended particulate matter (SPM)-associated Fe, Al, Zn, Cu, Cd, Cr, As, Pb and Co (a) at field site 1 (middle course; sampled 29.06.2017–31.06.2017) and (b) at field site 2 (estuary; sampled 01.07.2017–02.07.2017). Diurnal dynamics of SPM-associated HMs represented by content of metals quantified in fine-grained particles (0.45–8 μm), coarse-grained particles (>8 μm) and in their sum (>0.45 μm). Error bars represent standard deviations of triplicate water samples.

**Table 1**
Concentration of Fe, Al, Zn, Cu, Cd, Cr, As, Pb and Co determined in fine-grained suspended particulate matter (SPM; 0.45–8 μm), in coarse-grained SPM (>8 μm), in sum of fine- and coarse-grained SPM (>0.45 μm) and in dissolved state at field site 1 (middle course). Data shown as minimum, mean and maximum values and represent fluctuation in concentration of heavy metals within 48 h of sampling (29.06.2017–31.06.2017).

| Heavy metal | SPM-associated (μg/L) | | | | | | | | | Dissolved (mg/L) | | |
|---|---|---|---|---|---|---|---|---|---|---|---|---|
| | 0.45–8 μm | | | >8 μm | | | Sum (>0.45 μm) | | | | | |
| | Min. | Mean | Max. | Min. | Mean | Max. | Min. | Mean | Max. | Min. | Mean | Max. |
| Fe | 548.86 | 787.75 | 1001.16 | 555.18 | 829.97 | 1364.04 | 1305.76 | 1617.71 | 2148.24 | 1645.8 | 2003.28 | 2250.8 |
| Al | 1587.5 | 2201 | 2725 | 146.48 | 211.33 | 341.35 | 1770.3 | 2412.33 | 2991.35 | 589.6 | 718.48 | 787 |
| Zn | 65.76 | 83.29 | 99.38 | 34.19 | 41.85 | 55.83 | 103.68 | 125.14 | 150.19 | 212 | 279.18 | 347.2 |
| Cd | 0.22 | 0.43 | 2.15 | 0.13 | 0.16 | 0.21 | 0.37 | 0.59 | 2.33 | 0.85 | 0.99 | 1.08 |
| Cr | 0.03 | 0.49 | 1.53 | 0.07 | 0.16 | 0.59 | 0.14 | 0.65 | 1.89 | 0.001 | 0.003 | 0.006 |
| Cu | 24.96 | 47.02 | 60.16 | 17.2 | 20.58 | 25.28 | 45.5 | 67.57 | 85.44 | 124 | 149.7 | 171.4 |
| As | 0.69 | 0.97 | 1.42 | 1.03 | 2.43 | 5.6 | 2.21 | 3.41 | 6.3 | 1.23 | 1.43 | 1.61 |
| Pb | 1.68 | 3.74 | 13.31 | 1.36 | 4.94 | 16.86 | 3.33 | 8.68 | 21.25 | 0.03 | 0.04 | 0.05 |
| Co | 1.24 | 1.7 | 2.49 | 0.64 | 0.78 | 1.07 | 1.99 | 2.49 | 3.46 | 4.31 | 5.02 | 5.47 |

the influence of chlorine ions entering the estuary with seawater (Byrne et al., 2010; Rumin and Mironkina, 2013). In comparison with the river water, the estuarine water was also characterized by a decrease of SPM-associated Fe (from 1617.7 to 370.6 μg/L), Al (from 2412.3 to 152.4 μg/L), Zn (from 125.1 to 11.81 μg/L), Cu (from 67.6 to 8.16 μg/L), Cd (from 0.59 to 0.02 μg/L), Pb (from 8.7 to 3.51 μg/L) and Co (from 2.49 to 0.07 μg/L; Tables 1 and 2). However, the decrease in HM content was less pronounced for SPM-associated fraction. Furthermore, the concentrations of SPM-associated Cr (1.30 μg/L) and As (6.58 μg/L) were even higher in the estuary (Table 2).

The mean concentration values of HMs listed in Table 2 were used for calculation the percentage of metal distribution between fine-grained and coarse-grained SPM in the estuary water. The coarse-grained particles contained higher quantities of Fe (91.30%), Al (80.82%), Zn (65.33%), Cu (74.47%), As (96.16%) and Pb (89.87%). Cadmium (56.36%), Cr (51.87%) and Co (59.34%) were almost equally distributed between coarse-grained and fine-grained particles. We applied an identical approach for calculation the percentage of metal distribution between SPM-associated and dissolved fractions (Table 2). Obtained results suggest that in the estuary of the Rio Tinto, Fe (96.78%), Al (99.53%), Zn (99.84%), Cu (99.84%), Cd (99.93%), Pb (94.13%) and Co (99.94%) were predominantly dissolved in the water while up to 100% of As and Cr were associated with SPM during the whole tidal cycle. Thus, fluctuations of hydrochemical parameters contribute to essential removal of As and Cr from the estuarine water. Similar patterns were demonstrated earlier for the Rio Tinto and neighboring Odiel river (Cánovas et al., 2012a; Hierro et al., 2014).

The observed decrease in concentrations of dissolved Fe, Al, Zn, Cu, Co, Cd, As and Cr at field site 2 in comparison to field site 1 could be due to a combination of processes, including the dilution of the river water with the seawater upon mixing, leading to changes in salinity, Eh, bicarbonate content and consequently pH. These changes in geochemistry likely lead to the precipitation of HMs. Additionally, HMs can be precipitated due to evapoconcentration on the floodplain surrounding the estuary. The flocculation of solutes during rising of water salinity leads to enrichment of SPM-associated fraction with HMs (Mosley and Liss, 2019). Therefore, the content of SPM-associated HMs in the estuary water remained comparatively stable despite the seawater entering the estuary (Fig. 2b). Thus, tidal activity of the ocean contributes to periodical removal of solutes from the river water and either depositing them in the sediment or contributing to their washout as particles into the coastal ocean.

### *3.3. Mineral identity and elemental composition of SPM in the middle course of the Rio Tinto*

The mineralogical analysis of coarse-grained SPM showed the presence of both schwertmannite ($Fe_{16}O_{16}(OH)_{12}(SO_4)_2$) and ferrihydrite ($Fe_2O_3 \times 0.5(H_2O)$; Fig. 3a, f) which typically formed in mine impacted water bodies (Sánchez España et al., 2006). Linear combination fitting revealed that these two minerals accounted for 69.3% and 30.7% of the Fe minerals, respectively (Table A.1). Based on the Fe content in SPM (98 mg/g; Table 3) and the molar weight of schwertmannite and ferrihydrite (with Fe representing 57.81% and 66.21%, respectively), the SPM contained ca. 117.5 mg/g of schwertmannite and 45.4 mg/g of ferrihydrite. Among the other main elements in the SPM, we identified Al (146.2 mg/g of SPM; Table 3), which could be either incorporated into the structures of schwertmannite and ferrihydrite or form poorly crystalline aluminosilicates and Al (oxy)hydroxysulfates (Sánchez España et al., 2006; Manceau and Gates, 2013; Sánchez-España et al., 2016a). The high surface areas and a positive surface charge at low pH of these minerals can greatly impact the adsorption capacity of SPM towards cations and oxyanions such as $SO_4^{2-}$, As(III) and As(V) and therefore the transport of such metals (Cravotta, 2008; Campaner et al., 2014).

**Table 2**
Concentration of Fe, Al, Zn, Cu, Cd, Cr, As, Pb and Co determined in fine-grained suspended particulate matter (SPM; 0.45–8 μm), in coarse-grained SPM (>8 μm), in sum of fine- and coarse-grained SPM (>0.45 μm) and in dissolved state at field site 2 (estuary). Data shown as minimum, mean and maximum values and represent fluctuation in concentration of heavy metals within 24 h of sampling (01.07.2017–02.07.2017).

| Heavy metal | SPM-associated (μg/L) | | | | | | | | | Dissolved (mg/L) | | |
|---|---|---|---|---|---|---|---|---|---|---|---|---|
| | 0.45–8 μm | | | >8 μm | | | Sum (>0.45 μm) | | | | | |
| | Min. | Mean | Max. | Min. | Mean | Max. | Min. | Mean | Max. | Min. | Mean | Max. |
| Fe | 16.25 | 32.25 | 60.07 | 230.7 | 338.32 | 714.8 | 250.54 | 370.58 | 774.87 | 6.12 | 11.15 | 17.96 |
| Al | 14.52 | 29.23 | 65.71 | 63.46 | 123.17 | 224.15 | 82.83 | 152.4 | 248.13 | 16.88 | 32.41 | 45.76 |
| Zn | 1.93 | 4.09 | 7.2 | 4.93 | 7.72 | 13.93 | 7.65 | 11.81 | 21.13 | 3.64 | 7.16 | 10.6 |
| Cu | 1.3 | 2.08 | 3.47 | 4.55 | 6.08 | 8.14 | 6.73 | 8.16 | 11.61 | 2.92 | 5.04 | 6.84 |
| Cd | <0.005 | 0.01 | 0.05 | <0.005 | 0.01 | 0.04 | <0.005 | 0.02 | 0.08 | 0.02 | 0.03 | 0.05 |
| Cr | 0.54 | 0.63 | 0.74 | 0.29 | 0.68 | 2.36 | 0.87 | 1.3 | 3.07 | <0.0005 | <0.0005 | <0.0005 |
| As | 0.06 | 0.25 | 0.42 | 2.03 | 6.32 | 15.75 | 2.2 | 6.58 | 15.98 | <0.005 | <0.005 | <0.005 |
| Pb | 0.11 | 0.36 | 1.03 | 0.72 | 3.16 | 23.17 | 1.02 | 3.51 | 24.2 | 0.03 | 0.06 | 0.1 |
| Co | <0.005 | 0.04 | 0.1 | <0.005 | 0.03 | 0.12 | <0.005 | 0.07 | 0.22 | 0.05 | 0.12 | 0.24 |

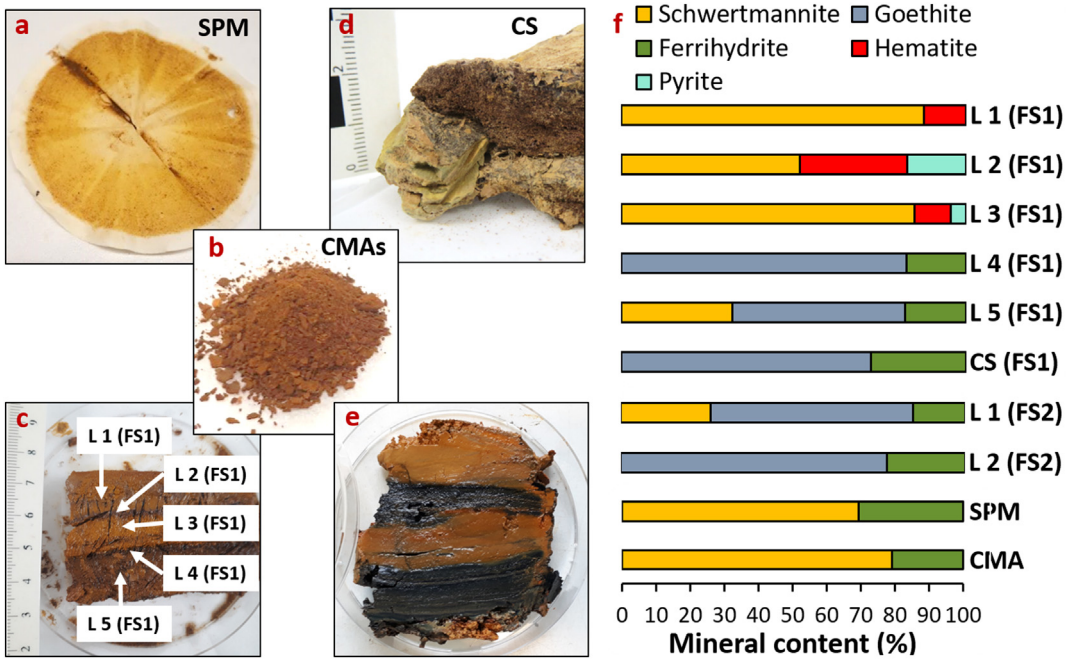


**Fig. 3.** Content of Fe minerals in the coarse-grained suspended particulate matter (SPM; >8 μm), microbially produced cell-Fe(III) mineral aggregates (CMAs) and sediments collected at field sites 1 and 2. a. Coarse-grained SPM sampled from field site 1. b. In vivo produced CMAs. c. Layered sediment with five distinct layers (L 1–L 5) from field site 1 (FS1). d. Underlying consolidated sediment (CS) sampled from field site 1. e. Layered sediment with two distinct layers (L 1 – orange layer and L 2 – black layer) sampled from field site 2. f. Results of the LCF of Fe K-edge EXAFS spectra for all samples. Fe K-edge EXAFS spectra plotted in k space and the corresponding linear combination fits are shown in the Fig. A.2. Standards used in LCF and principle component analysis are shown in the Fig. A.3. (For interpretation of the references to color in this figure legend, the reader is referred to the web version of this article.)

However, these ions can be remobilized later due to microbial reduction or photoreduction of particulate Fe(III) minerals (González-Toril et al., 2003; Diez et al., 2009; Egal et al., 2009). The release of Fe(II) from SPM can be a relevant in the control of Fe(II) content along the Rio Tinto and therefore support activity of Fe(II)-oxidizing microorganisms at the distance from open-pit mines, waste-rock piles, tailings and naturally exposed outcrops of sulfides.

### *3.4. Formation of Fe(III) minerals mediated by acidophilic Fe(II)-oxidizing microorganisms*

The precipitation of minerals in the northern zone of the Rio Tinto occurs after microbially modulated oversaturation of the water with Fe(III). In the river water, >60% of 16S rRNA gene sequences belonged to Fe(II)-oxidizing *Acidithiobacillus* spp. and *Leptospirillum* spp. while >10% belonged to Fe(III)-reducing *Acidiphilium* spp. and *Acidibacter* spp. (Fig. 4a). These Fe-metabolizing acidophiles are the main organisms responsible for Fe cycling in the river (González-Toril et al., 2003; Méndez-García et al., 2015). *Acidithiobacillus* spp. and *Leptospirillum* spp. mediate Fe(II) oxidation in the oxic zones of the river, while *Acidiphilium* spp. and *Acetobacter* spp. are responsible for Fe(III) reduction in the oxic and anoxic zones, as well for consumption of organic matter, which can inhibit chemolithoautotrophic growth of *Acidithiobacillus* spp. and *Leptospirillum* spp. (Liu et al., 2011; Johnson et al., 2012; Falagan and Johnson, 2014). The same microorganisms were found associated with coarse-grained particles, suggesting that Fe(III) could also be precipitated at the cell surface or in close vicinity of the cells leading to the formation of cell-Fe(III) mineral aggregates (CMAs).

In order to evaluate the formation of CMAs and their impact on HM mobility, an Fe(II)-oxidizing microbial consortium from the river water was isolated and further investigated. DNA extraction followed by 16S rRNA gene sequencing showed that this consortium is dominated by *Acidithiobacillus* spp. and the *Acidiphilium* spp. (87.3% and 11.6% of total sequences, respectively; Fig. 4a). Cultivation of this consortium in acidic medium (pH 2.3) containing 2.5 g/L of Fe(II) led to complete oxidation of the Fe(II) within 4 days, reaching $1.7 \times 10^7$ cells/mL (Fig. 4b) with an oxidation rate of 25.6 μg Fe(II)/min × $10^9$ cells (Fig. A.4). The Fe

**Table 3**
Weight distribution of Fe, Al, Zn, Cu, Cd, As, Cr, Pb, Co, and Si between suspended particulate matter (SPM) and sediment at both field sites. Data shown as mean value of triplicate samples for sediment layers and consolidated sediment (CS) and as a mean value of 24 samples for SPM from field site 1 and 12 samples from field site 2. BDL - below detection limit; na – not applicable.

| Field site | Sample | Elemental content | | | | | | | | | |
|---|---|---|---|---|---|---|---|---|---|---|---|
| | | Fe (mg/g) | Al (mg/g) | Zn (mg/g) | Cu (mg/g) | Cd (μg/g) | As (mg/g) | Cr (μg/g) | Pb (mg/g) | Co (μg/g) | Si (mg/g) |
| Middle course | SPM | 98.1 | 146.2 | 7.6 | 4.1 | 40 | 0.21 | 40 | 0.53 | 150 | na |
| | Layer 1 | 501 | 39.1 | 0.8 | 0.67 | 7 | 9.1 | 60 | 12.3 | 2.3 | 117.2 |
| | Layer 2 | 406.4 | 107.4 | 2.07 | 1.77 | 10 | 16.4 | 90 | 30.8 | 23 | 49.2 |
| | Layer 3 | 623.5 | 17.4 | 0.32 | 0.23 | 6 | 5.69 | 15 | 4.04 | BDL | 23.3 |
| | Layer 4 | 540.3 | 44.9 | 0.39 | 0.44 | 5.5 | 4.2 | 25 | 4.29 | 1.3 | 99.3 |
| | Layer 5 | 504.3 | 62.6 | 0.66 | 0.59 | 5.7 | 6.9 | 43 | 7 | 16 | 105.7 |
| | CS | 295.6 | 155.3 | 0.21 | 0.32 | 1.3 | 1.6 | 110 | 1.23 | BDL | 40.4 |
| Estuary | SPM | 7.12 | 2.93 | 0.23 | 0.16 | 0.4 | 0.13 | 30 | 0.07 | 1.3 | na |
| | Layer 1 | 219.1 | 163.1 | 0.659 | 1.29 | 3 | 1 | 20 | 1.6 | 10 | 227 |
| | Layer 2 | 142.9 | 217.3 | 6.2 | 6.1 | 35 | 1.5 | 40 | 2.088 | 60 | 226 |

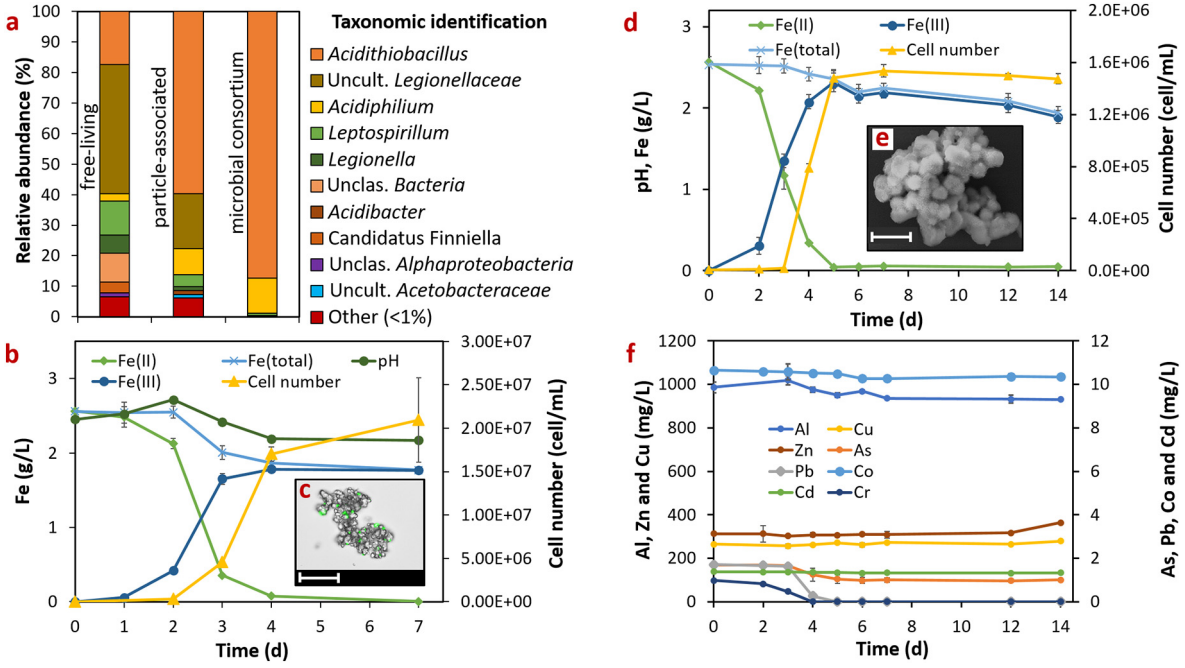


**Fig. 4.** Taxonomic identification, growth parameters and heavy metal immobilization potential of the Fe(II)-oxidizing microbial consortium, isolated from the water of the middle course of the Rio Tinto. a. DNA-based 16S rRNA gene sequence abundance of microbial taxa, identified as free-living (collected with 0.22 μm pore size filter) and particle-associated (collected with 8 μm pore size filter) microorganisms in the river water at field site 1 and from the Fe(II)-oxidizing microbial consortium. b. Dynamics of Fe(II) oxidation and cell number in a growing Fe (II)-oxidizing culture. c. Light microscopy image of cell-Fe(III) mineral aggregates formed during oxidation of Fe(II) by the microbial consortium stained with SYTO 9. Green color represents cells of the enrichment culture associated with mineral particles (grey/black). White bar corresponds to 25 μm. d. Dynamics of Fe(II) oxidation in a growing Fe(II)-oxidizing culture in the presence of Al, Zn, Pb, Cd, Cu, As, Co and Cr. e. SEM image showing individual schwertmannite globules (ca. 2 μm in diameter). White bar corresponds to 5 μm. f. Behavior of Al, Zn, Pb, Cd, Cu, As, Co and Cr in a growing Fe(II)-oxidizing culture. Uninoculated control samples for both cultivation experiments were incubated at the same geochemical conditions (Fig. A.5). Error bars in b, d and f diagrams represent standard deviations of triplicate bottles. (For interpretation of the references to color in this figure legend, the reader is referred to the web version of this article.)

(II) content in abiotic (i.e. uninoculated) controls remained constant since abiotic Fe(II) oxidation at pH values lower than five is kinetically inhibited (Morgan and Lahav, 2007). Microbial oxidation of Fe(II) led to an oversaturation in Fe(III) and a consumption of $H^+$ by $O_2$ reduction (Eq. (1)), causing a pH increase to 2.7. The precipitation of 0.69 g of the Fe(III) (27% of the total Fe) led to $H^+$ release and to a pH stabilization at around 2.2 (Eqs. (2) and (3)). The cell surfaces may have accelerated Fe (III) mineral precipitation by providing nucleation sites which lower the activation energy kinetically, facilitating mineral cluster nucleation at the cell surface (Duquesne et al., 2003; Sánchez-España et al., 2016b). Precipitation of Fe(III) minerals associated with cells led to the formation of CMAs (Fig. 4c). Mineralogical analysis of the CMAs revealed a combination of schwertmannite and ferrihydrite (Fig. 3b, f).

### 3.5. Co-precipitation of heavy metals by microbially produced Fe(III) minerals

The formation of CMAs can play a key role for immobilization of HMs. In order to evaluate this contribution, the Fe(II)-oxidizing consortium was incubated in medium supplemented by in situ concentrations of Al, Zn, Cu, Co, Pb, As, Cd and Cr. The cell yield in the stationary growth phase was ca. 10-fold lower in the presence of the HMs (Fig. 4d) compared to medium without HM load (Fig. 4b) due to partial consumption of energy by HM detoxification mechanisms instead of biosynthesis (Dopson et al., 2003; Navarro et al., 2013). The oxidation of 1.4 g/L of Fe(II) led to an oversaturation of the medium with Fe(III) followed by precipitation of 0.3 g (11.8%) of the Fe(III) as minerals (Fig. 4e). It was ca. 2-fold lower in absolute amount than in the medium without HMs. The reason for the lower amount of Fe(III) precipitation in the HM-amended medium could be the 10-fold lower cell number caused by toxicity and, therefore, the lower number of available nucleation sites.

During microbial Fe(II) oxidation, the HMs present were co-precipitated to various degrees depending on the Fe(III) mineral precipitation and on identity of the HM (Fig. 4f). Dissolved concentrations of Pb and As (1.7 mg/L each) as well as Cr (0.1 mg/L) remained almost unchanged for the first 3 days of cultivation when no Fe(III) mineral precipitation was observed. Precipitation of Fe(III) minerals on days 4–5 was accompanied by removal of Pb and Cr from solution. The complete removal of Pb and Cr in agreement with the high content of these metals in the SPM sampled from field site 1 (Table 1). Arsenic concentration was reduced to 0.98 mg/L by day 6 (when Fe(II) oxidation was complete) and then remained almost stable until the end of incubation (day 14). Precipitation of As is common for acidic environments (Paikaray, 2015; Park et al., 2016). The predominant aqueous species of As and Cr are anions ($AsO_4^{3-}$ and $CrO_4^{2-}$). In these forms they can be sorbed by positively charged surfaces of Fe(III) minerals or can substitute $SO_4^{2-}$ in schwertmannite due to similar tetrahedrally coordination and ionic radius (Regenspurg et al., 2004; España et al., 2005; Regenspurg and Peiffer, 2005; Sánchez España et al., 2006; Burton et al., 2009). Although the critical pH range for sorption of Pb is commonly comprised between 3 and 5, it can react with $SO_4^{2-}$ and precipitate as Pb sulfates (e.g. anglesite; $PbSO_4$) which has low solubility in low-pH, $SO_4^{2-}$-rich solutions (Smith, 1999; Wang et al., 2013).

In contrast to Cr, Pb and As, the dissolved concentrations of the Co and Cd were only affected to a small extent by Fe(III) mineral precipitation. Cobalt (initial concentration of 21.28 mg/L) decreased slightly to 20.70 mg/L at the end of Fe(II) oxidation while Cd was reduced from 1.39 mg/L to 1.35 mg/L. Similarly, appreciable removal of Cu and Zn from solution during the incubation was not observed. For Al, the initial concentration of 0.98 g/L decreased to 0.93 g/L during incubation, showing that ca. 50 mg/L was co-precipitated. Aluminum, Cu, Zn, Co and Cd behave conservatively under acidic conditions and therefore remained dissolved even in the presence of available nucleation sites (España et al., 2005). Thus, noticeable removal of these metals occurred during Fe(III) mineral precipitation but not after this precipitation. This trend suggests that the low pH of the medium prevented later sorption of

cations to the surface of the Fe(III) minerals, due to the electrostatic repulsion between the metal cations and the positive surface charge of the CMAs (e.g. $Fe(OH)^{2+}$; Bonnissel-Gissinger et al., 1998; Sánchez España et al., 2006).

### 3.6. Contribution of SPM to sediment formation and heavy metal burial

Depending on river flow rate, grain size and density, SPM consisting of minerals, organic matter and HMs are either deposited in the sediment (at low flow rate) or circulated up from the sediment (at high flow rate). In case of deposition of SPM, the sediment can be considered as an important sink for HMs and the further fate of HMs depends on biological processes (e.g. remobilization of HMs due to microbial Fe(III) reduction) and physical processes (e.g. mineral transformations, sediment mixing; Küsel et al., 1999; Lynch et al., 2014). To examine the fate of HMs in sediment, specimens were collected from field site 1. In order to determine the mineral identity and elemental composition of the sediment, the specimen was sliced into five distinct layers formed under different hydro(bio)geochemical conditions (Fig. 3c). Mineralogical analysis revealed a gradual transformation of metastable schwertmannite and ferrihydrite to more crystalline goethite and hematite in different sediment layers and more consolidated sediment underneath (Fig. 3d, f). This mineralogy suggests that SPM consisting of schwertmannite and ferrihydrite form the primary sediment, where dehydration and recrystallization likely led to the progressive transformation of poorly ordered phases into more crystalline Fe(III) minerals (Fernández-Remolar et al., 2003; Jiménez et al., 2019). High concentrations of Si and Al in the sediment (Table 3) suggest the presence of aluminosilicates, which likely have undergone a similar crystallization process (González-Toril et al., 2003). Crystallization of minerals and their following compaction potentially led to the formation of more consolidated sediment, mainly consisting of schwertmannite and goethite. Schwertmannite could have been protected from the transformation to more crystalline minerals by stabilization via sorption of sulfate, protons, silicate or natural organic matter to the mineral surface (Collins et al., 2010). During crystallization of sediments, part of the HMs remained associated with the bulk minerals, as evidenced by the analysis of trace metals in SPM. These HM-rich SPM eventually contribute to the formation of the more consolidated sediment, where constant pathways of Cr, Al and to a lesser extent As, Pb, Zn, Cu and Cd were identified (Table 3).

In contrast to field site 1, in the estuary of the river massive sediment deposition characterized by layered structures with distinct orange and black zones was observed (Fig. 3e). We identified schwertmannite, goethite and ferrihydrite as the main Fe minerals in both zones (Fig. 3f). Based on the high Fe content in the sediment (219.1 mg/g in orange and 142.9 mg/g in black material) it is plausible that schwertmannite, goethite and ferrihydrite are the main constituents of this sediment transported to the estuary with a river flow. Additionally, a high content of Al (163.1 and 217.3 mg/g) and Si (227 mg/g and 226 mg/g) in both layers suggests the presence of aluminosilicates which could be transported from the northern zone or be flocculated directly in the estuary due to the increase of pH and salinity values. The black zone of the sediment can be inhabiting by sulfate-reducing bacteria (SRB) responsible for sulfide formation and Fe(III) mineral transformation (Velasco et al., 2011). Attachment of SRB to the mineral and formation of biofilms can help to reduce HM toxicity (Lin et al., 2013; Castro et al., 2019). For example, release of extracellular polymeric substances can complex and detoxify HMs (e.g. Cu). The complexed metals can be then precipitated as metal sulfides (Sani et al., 2001).

Abiotically induced precipitation of minerals in the estuary as well as deposition of SPM transported from the northern zone led to an accumulation of HMs in the top sediment layer (Table 3). However, the concentration of all HMs, except Fe, was found to be higher in the black

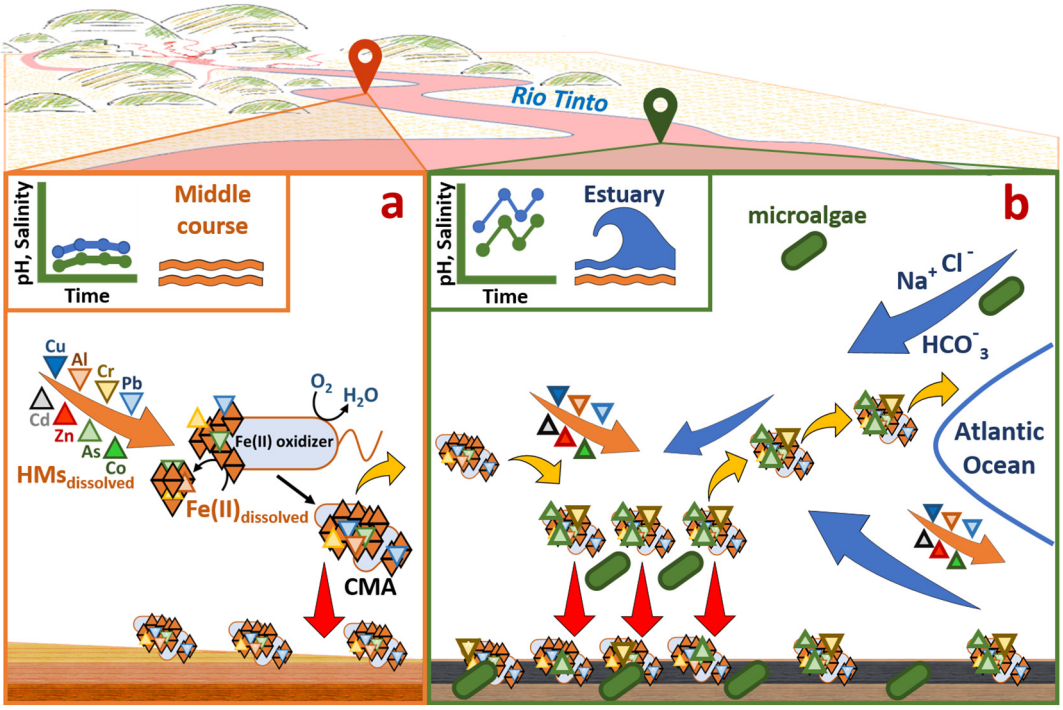


**Fig. 5.** Simplified model of heavy metal (HM) behavior in the middle course and estuary of the Rio Tinto demonstrating the role of the suspended particulate matter (SPM) in transport of HMs into the coastal ocean (longitudinal pathway; yellow arrows) and into the river sediment (sedimentation pathway; red arrows). a. Oxidation of Fe(II) leads to oversaturation of Fe(III) in the water of the middle course of the river and precipitation of microbially produced Fe(III) at the nucleation sites (e.g. extracellular polymeric substance) at the surface of microbial cells and to formation of cell-Fe(III) mineral aggregates (CMAs). Part of the CMAs finally precipitates contributing to formation of layered sediment and burial of HMs while another part remains suspended in the water column. b. SPM consisting of CMAs is transported to the estuary, where tidal mixing events (blue arrows) lead to abiotic precipitation of Fe(III) oxyhydroxides and co-precipitation of HMs. All newly formed mineral particles associated with HMs as well microbial and microalgal cells replenish the pool of SPM. A part of SPM ends up in the fluvial-estuarine sediment, while another part eventually enters the coastal ocean. (For interpretation of the references to color in this figure legend, the reader is referred to the web version of this article.)

zone (i.e. below 2 cm) than in the top orange layer. Diurnal and seasonal hydrogeochemical fluctuations could facilitate the recrystallization of metastable minerals and the partial remobilization of HMs in the top sediment. Sulfate-reducing bacteria inhabiting the anoxic, sulfate- and organic matter-rich zones probably caused the conversion of sulfate to sulfide, which reacted with the HMs and precipitated them as metal sulfides or immobilized them on Fe(II) sulfides (Ayangbenro et al., 2018). These stable metal sulfides could therefore serve as a sink for HMs, as it was observed for example, for Pb, As, Cd and Zn (2.09 mg/g, 1.5 mg/g, 35 μg/g and 6.2 mg/g, respectively).

## 4. Environmental implications

Detailed water analysis demonstrated that HMs (e.g. As, Pb and Cr) were associated with suspended schwertmannite- and ferrihydrite-containing particles, constantly forming in the water column due to microbial Fe(II) oxidation. After formation, SPM maintains two divergent but interrelated pathways of HMs. The first, longitudinal pathway provides continuous transport of SPM-associated HMs into the river estuary where SPM is enriched with floccules, evaporites and marine phytoplankton (Fig. 5). From the estuary, tidal water can transport SPM-associated HMs to the ocean, where they could end up in the coastal sediment or could be spread with sea currents across the Gulf of Cadiz. The second, sedimentation pathway provides continuous burial of HMs in the sediment throughout the river. In the middle course, the sediment is progressively transforming into more consolidated material and traps HMs within the structure of minerals while in the estuary HMs are retained in anoxic clay minerals. These two SPM-associated pathways play an important role for the mobility of HMs (particularly Pb, As and Cr) in the Rio Tinto.

## CRediT authorship contribution statement

**Sergey M. Abramov:** Conceptualization, Methodology, Formal analysis, Investigation, Writing - original draft, Visualization, Project administration. **Julian Tejada:** Investigation, Resources. **Lars Grimm:** Investigation. **Franziska Schädler:** Investigation. **Aleksandr Bulaev:** Investigation, Resources. **Elizabeth J. Tomaszewski:** Formal analysis, Investigation, Visualization. **James M. Byrne:** Formal analysis. **Daniel Straub:** Formal analysis, Data curation, Visualization. **Harald Thorwarth:** Resources. **Ricardo Amils:** Methodology, Supervision. **Sara Kleindienst:** Conceptualization, Methodology, Supervision, Funding acquisition. **Andreas Kappler:** Conceptualization, Methodology, Supervision, Project administration, Funding acquisition.

## Declaration of competing interest

The authors declare that they have no known competing financial interests or personal relationships that could have appeared to influence the work reported in this paper.

## Acknowledgments

We acknowledge Ellen Röhm, Julian Sorwat, Timm Bayer, Dr. Nia Blackwell and Dr. Heinrich Taubald for technical support and discussions. This study was supported by a grant from the German Research Foundation (DFG) to Andreas Kappler (KA 1736/43-1). Daniel Straub is funded by the Institutional Strategy of the University of Tübingen (DFG, ZUK 63) and further supported by the Collaborative Research Center 1253 CAMPOS (DFG, Grant Agreement SFB 1253/1 2017). Sara Kleindienst is funded by an Emmy-Noether fellowship (DFG, grant No 326028733). This study also used resources of the Advanced Photon Source, a U.S. Department of Energy (DOE) Office of Science User Facility operated for the DOE Office of Science by Argonne National Laboratory under Contract No. DE-AC02-06CH11357. EXAFS analysis was completed at the new MRCAT (Sector 10) bending magnet and insertion device beamlines at the Advanced Photon source. MRCAT operations are supported by the Department of Energy and the MRCAT member institutions. We would like to thank Dr. Joshua Wright (APS), Dr. Sarah Balgooyen, Emma Trainer and Lily Schacht for help with data collection.

## Appendix A. Supplementary data

Supplementary data to this article can be found online at https://doi.org/10.1016/j.scitotenv.2020.137294.

## References

Achterberg, E.P., Herzl, V.M.C., Braungardt, C.B., Millward, G.E., 2003. Metal behavior in an estuary polluted by acid mine drainage: the role of particulate matter. Environ. Pollut. 121 (2), 283–292. https://doi.org/10.1016/s0269-7491(02)00216-6.

Altaee, A., Alanezi, A.A., Hawari, A.H., 2018. Forward osmosis feasibility and potential future application for desalination. In: Gude, V.G. (Ed.), Emerging Technologies for Sustainable Desalination Handbook. Butterworth-Heinemann, pp. 35–54.

Amils, R., González-Toril, E., Fernández-Remolar, D., Gómez, F., Aguilera, Á., Rodríguez, N., Malki, M., García-Moyano, A., Fairén, A.G., de la Fuente, V., Luis Sanz, J., 2007. Extreme environments as Mars terrestrial analogs: the Rio Tinto case. Planet. Space Sci. 55 (3), 370–381. https://doi.org/10.1016/j.pss.2006.02.006.

Ayangbenro, A.S., Olanrewaju, O.S., Babalola, O.O., 2018. Sulfate-reducing bacteria as an effective tool for sustainable acid mine bioremediation. Front. Microbiol. 9 (1986). https://doi.org/10.3389/fmicb.2018.01986.

Bonnissel-Gissinger, P., Alnot, M., Ehrhardt, J.-J., Behra, P., 1998. Surface oxidation of pyrite as a function of pH. Environ. Sci. Technol. 32 (19), 2839–2845. https://doi.org/10.1021/es980213c.

Borrego, J., Morales, J., de la Torre, M., Grande, J., 2002. Geochemical characteristics of heavy metal pollution in surface sediments of the Tinto and Odiel River estuary (southwestern Spain). Environ. Geol. 41 (7), 785–796. https://doi.org/10.1007/s00254-001-0445-3.

Braungardt, C.B., Achterberg, E.P., Elbaz-Poulichet, F., Morley, N.H., 2003. Metal geochemistry in a mine-polluted estuarine system in Spain. Appl. Geochem. 18 (11), 1757–1771. https://doi.org/10.1016/S0883-2927(03)00079-9.

Burton, E.D., Bush, R.T., Johnston, S.G., Watling, K.M., Hocking, R.K., Sullivan, L.A., Parker, G.K., 2009. Sorption of arsenic(V) and arsenic(III) to schwertmannite. Environ. Sci. Technol. 43 (24), 9202–9207. https://doi.org/10.1021/es902461x.

Byrne, R.H., Yao, W., Luo, Y., Millero, F.J., 2010. Complexation of Pb(II) by chloride ions in aqueous solutions. Aquat. Geochem. 16 (3), 325–335. https://doi.org/10.1007/s10498-010-9101-4.

Campaner, V.P., Luiz-Silva, W., Machado, W., 2014. Geochemistry of acid mine drainage from a coal mining area and processes controlling metal attenuation in stream waters, southern Brazil. An. Acad. Bras. Cienc. 86, 539–554. https://doi.org/10.1590/0001-37652014113712.

Cánovas, C.R., Olias, M., Vazquez-Suñé, E., Ayora, C., Nieto, J.M., 2012a. Influence of releases from a fresh water reservoir on the hydrochemistry of the Tinto River (SW Spain). Sci. Total Environ. 416, 418–428. https://doi.org/10.1016/j.scitotenv.2011.11.079.

Cánovas, C.R., Olías, M., Sarmiento, A.M., Nieto, J.M., Galván, L., 2012b. Pollutant transport processes in the Odiel River (SW Spain) during rain events. Water Resour. Res. 48, w06508. https://doi.org/10.1029/2011WR011041.

Caporaso, J.G., Kuczynski, J., Stombaugh, J., Bittinger, K., Bushman, F.D., Costello, E.K., Fierer, N., Peña, A.G., Goodrich, J.K., Gordon, J.I., Huttley, G.A., Kelley, S.T., Knights, D., Koenig, J.E., Ley, R.E., Lozupone, C.A., McDonald, D., Muegge, B.D., Pirrung, M., Reeder, J., Sevinsky, J.R., Turnbaugh, P.J., Walters, W.A., Widmann, J., Yatsunenko, T., Zaneveld, J., Knight, R., 2010. QIIME allows analysis of high-throughput community sequencing data. Nat. Methods 7, 335. https://doi.org/10.1038/nmeth.f.303.

Castro, L., Blázquez, M.L., González, F., Muñoz, J.A., Ballester, A., 2019. Anaerobic bioreduction of jarosites and biofilm formation by a natural microbial consortium. Minerals 9, 81. https://doi.org/10.3390/min9020081.

Collins, R.N., Jones, A.M., Wite, T.D., 2010. Schwertmannite stability in acidified coastal environments. Geochim. Cosmochim. Ac. 74 (2), 482–496. https://doi.org/10.1016/j.gca.2009.10.014.

Cravotta, C.A., 2008. Dissolved metals and associated constituents in abandoned coal-mine discharges, Pennsylvania, USA. Part 1: constituent quantities and correlations. Appl. Geochem. 23 (2), 166–202. https://doi.org/10.1016/j.apgeochem.2007.10.011.

Davis Jr., R.A., Welty, A.T., Borrego, J., Morales, J.A., Pendon, J.G., Ryan, J.G., 2000. Rio Tinto estuary (Spain): 5000 years of pollution. Environ. Geol. 39 (10), 1107–1116. https://doi.org/10.1007/s002549900.

de la Torre, M.L., Sánchez-Rodas, D., Grande, J.A., Gomez, T., 2010. Relationships between pH, colour and heavy metal concentrations in the Tinto and Odiel rivers (southwest Spain). Hydrol. Res. 41 (5), 406–413. https://doi.org/10.2166/nh.2010.082.

Diez, E.M., López, P.E., Sánchez España, J., 2009. Aquat. Geochem. 15, 391–419. https://doi.org/10.1007/s10498-008-9044-1.

Dold, B., 2014. Evolution of acid mine drainage formation in sulphidic mine tailings. Minerals 4 (3), 621–641. https://doi.org/10.3390/min4030621.

Dopson, M., Baker-Austin, C., Koppineedi, P.R., Bond, P.L., 2003. Growth in sulfidic mineral environments: metal resistance mechanisms in acidophilic microorganisms. Microbiol 149 (8), 1959–1970. https://doi.org/10.1099/mic.0.26296-0.

Duquesne, K., Lebrun, S., Casiot, C., Bruneel, O., Personné, J.-C., Leblanc, M., Elbaz-Poulichet, F., Morin, G., Bonnefoy, V., 2003. Immobilization of arsenite and ferric iron by *Acidithiobacillus ferrooxidans* and its relevance to acid mine drainage. Appl.

Environ. Microbiol. 69 (10), 6165–6173. https://doi.org/10.1128/AEM.69.10.6165-6173.2003.
Egal, M., Casiot, C., Morin, G., Parmentier, M., Bruneel, O., Lebrun, S., Elbaz-Poulichet, F., 2009. Kinetic control on the formation of tooeleite, schwertmannite and jarosite by *Acidithiobacillus ferrooxidans* strains in an As(III)-rich acid mine water. Chem. Geol. 265 (3), 432–441. https://doi.org/10.1016/j.chemgeo.2009.05.008.
Elbaz-Poulichet, F., Leblanc, M., Borrego, J., Morales, J.A., 2000. 4,500-Year-old mining pollution in southwestern Spain: long-term implications for modern mining pollution. Econ. Geol. 95 (3), 655–662. https://doi.org/10.2113/gsecongeo.95.3.655.
Elbaz-Poulichet, F., Braungardt, C., Achterberg, E., Morley, N., Cossa, D., Beckers, J.-M., Nomérange, P., Cruzado, A., Leblanc, M., 2001. Metal biogeochemistry in the Tinto–Odiel rivers (Southern Spain) and in the Gulf of Cadiz: a synthesis of the results of TOROS project. Cont. Shelf Res. 21 (18), 1961–1973. https://doi.org/10.1016/S0278-4343(01)00037-1.
España, J.S., Pamo, E.L., Pastor, E.S., Andrés, J.R., Rubí, J.A.M., 2005. The natural attenuation of two acidic effluents in Tharsis and La Zarza-Perrunal mines (Iberian Pyrite Belt, Huelva, Spain). Environ. Geol. 49 (2), 253–266. https://doi.org/10.1007/s00254-005-0083-2.
Falagan, C., Johnson, D.B., 2014. *Acidibacter ferrireducens* gen. nov., sp. nov.: an acidophilic ferric iron-reducing gammaproteobacterium. Extremophiles 18 (6), 1067–1073. https://doi.org/10.1007/s00792-014-0684-3.
Fernández-Remolar, D.C., Rodriguez, N., Gómez, F., Amils, R., 2003. Geological record of an acidic environment driven by iron hydrochemistry: the Tinto River system. J. Geophys. Res. Planets 108 (E7), 5080. https://doi.org/10.1029/2002JE001918.
González-Toril, E., Llobet-Brossa, E., Casamayor, E.O., Amann, R., Amils, R., 2003. Microbial ecology of an extreme acidic environment, the Tinto River. Appl. Environ. Microbiol. 69 (8), 4853–4865. https://doi.org/10.1128/aem.69.8.4853-4865.2003.
Hierro, A., Olías, M., Cánovas, C.R., Martín, J.E., Bolivar, J.P., 2014. Trace metal partitioning over a tidal cycle in an estuary affected by acid mine drainage (Tinto estuary, SW Spain). Sci. Total Environ. 497-498, 18–28. https://doi.org/10.1016/j.scitotenv.2014.07.070.
Jiménez, A., Hernández, A., Prieto, M., 2019. Crystallization behaviour of iron-hydroxide sulphates by aging under ambient temperature conditions. Minerals 9 (1), 27. https://doi.org/10.3390/min9010027.
Johnson, D.B., Kanao, T., Hedrich, S., 2012. Redox transformations of iron at extremely low ph: fundamental and applied aspects. Front. Microbiol. 3, 96. https://doi.org/10.3389/fmicb.2012.00096.
Küsel, K., Dorsch, T., Acker, G., Stackebrandt, E., 1999. Microbial reduction of Fe(III) in acidic sediments: isolation of *Acidiphilium cryptum* JF-5 capable of coupling the reduction of Fe(III) to the oxidation of glucose. Appl. Environ. Microbiol. 65 (8), 3633–3640.
Lin, T.Y., Kampalath, R.A., Lin, C.-C., Zhang, M., Chavarria, K., Lacson, J., Jay, J.A., 2013. Investigation of mercury methylation pathways in biofilm versus planktonic cultures of *Desulfovibrio desulfuricans*. Environ. Sci. Technol. 47 (11), 5695–5702. https://doi.org/10.1021/es400079n.
Liu, H., Yin, H., Dai, Y., Dai, Z., Liu, Y., Li, Q., Jiang, H., Liu, X., 2011. The co-culture of *Acidithiobacillus ferrooxidans* and *Acidiphilium acidophilum* enhances the growth, iron oxidation, and $CO_2$ fixation. Arch. Microbiol. 193 (12), 857–866. https://doi.org/10.1007/s00203-011-0723-8.
Lueders, T., Manefield, M., Friedrich, M.W., 2004. Enhanced sensitivity of DNA- and rRNA-based stable isotope probing by fractionation and quantitative analysis of isopycnic centrifugation gradients. Environ. Microbiol. 6 (1), 73–78. https://doi.org/10.1046/j.1462-2920.2003.00536.x.
Lynch, F.S., Batty, C.L., Byrne, P., 2014. Environmental risk of metal mining contaminated river bank sediment at redox-transitional zones. Minerals 4, 52–73. https://doi.org/10.3390/min4010052.
Manceau, A., Gates, W.P., 2013. Incorporation of Al in iron oxyhydroxides: implications for the structure of ferrihydrite. Clay Miner. 48 (3), 481–489. https://doi.org/10.1180/claymin.2013.048.3.05.
Méndez-García, C., Peláez, A.I., Mesa, V., Sánchez, J., Golyshina, O.V., Ferrer, M., 2015. Microbial diversity and metabolic networks in acid mine drainage habitats. Front. Microbiol. 6, 475. https://doi.org/10.3389/fmicb.2015.00475.
Morgan, B., Lahav, O., 2007. The effect of pH on the kinetics of spontaneous Fe(II) oxidation by $O_2$ in aqueous solution - basic principles and a simple heuristic description. Chemosphere 68 (11), 2080–2084. https://doi.org/10.1016/j.chemosphere.2007.02.015.
Mosley, L.M., Liss, P.S., 2019. Particle aggregation, pH changes and metal behaviour during estuarine mixing: review and integration. Mar. Freshw. Res. https://doi.org/10.1071/MF19195.
Ñancucheo, I., Rowe, O.F., Hedrich, S., Johnson, D.B., 2016. Solid and liquid media for isolating and cultivating acidophilic and acid-tolerant sulfate-reducing bacteria. FEMS Microbiol. Lett. 363 (10), fnw083. https://doi.org/10.1093/femsle/fnw083.
Navarro, C.A., von Bernath, D., Jerez, C.A., 2013. Heavy metal resistance strategies of acidophilic bacteria and their acquisition: importance for biomining and bioremediation. Biol. Res. 46 (4), 363–371. https://doi.org/10.4067/s0716-97602013000400008.
Neff, J.M., 2002. Chapter 7 - chromium in the ocean. In: Neff, J.M. (Ed.), Bioaccumulation in marine organisms. Elsevier, Oxford, pp. 131–143.
Nieto, J.M., Sarmiento, A.M., Olías, M., Canovas, C.R., Riba, I., Kalman, J., Delvalls, T.A., 2007. Acid mine drainage pollution in the Tinto and Odiel rivers (Iberian Pyrite Belt, SW Spain) and bioavailability of the transported metals to the Huelva estuary. Environ. Int. 33 (4), 445–455. https://doi.org/10.1016/j.envint.2006.11.010.
Nieto, J.M., Sarmiento, A.M., Canovas, C.R., Olias, M., Ayora, C., 2013. Acid mine drainage in the Iberian Pyrite Belt: 1. hydrochemical characteristics and pollutant load of the Tinto and Odiel rivers. Environ. Sci. Pollut. Res. Int. 20 (11), 7509–7519. https://doi.org/10.1007/s11356-013-1634-1639.
Olías, M., Nieto, J.M., 2015. Background conditions and mining pollution throughout history in the Río Tinto (SW Spain). Environ 2, 295–316. https://doi.org/10.3390/environments2030295.
Paikaray, S., 2015. Arsenic geochemistry of acid mine drainage. Mine Water Environ. 34 (2), 181–196. https://doi.org/10.1007/s10230-014-0286-4.
Park, J.H., Han, Y.S., Ahn, J.S., 2016. Comparison of arsenic co-precipitation and adsorption by iron minerals and the mechanism of arsenic natural attenuation in a mine stream. Water Res. 106, 295–303. https://doi.org/10.1016/j.watres.2016.10.006.
Periáñez, R., 2013. Water circulation, sediment transport, and pollutant dynamics in southern Iberia waters: a review on numerical modelling studies. ISRN Oceanography vol. 2013. https://doi.org/10.5402/2013/424572 Article ID 424572, 27 p.
Ravel, B., Newville, M., 2005. ATHENA, ARTEMIS, HEPHAESTUS: data analysis for X-ray absorption spectroscopy using IFEFFIT. J. Synchrotron Radiat., 12 (Pt 4), 537–541. doi: https://doi.org/10.1107/S0909049505012719.
Regenspurg, S., Peiffer, S., 2005. Arsenate and chromate incorporation in schwertmannite. Appl. Geochem. 20 (6), 1226–1239. https://doi.org/10.1016/j.apgeochem.2004.12.002.
Regenspurg, S., Brand, A., Peiffer, S., 2004. Formation and stability of schwertmannite in acidic mining lakes. Geochim. Cosmochim. Acta 68 (6), 1185–1197. https://doi.org/10.1016/j.gca.2003.07.015.
Rumin, A.I., Mironkina, N.V., 2013. Study of dissolution kinetics of lead sulfate in solutions of sodium chloride and sodium hydrate. J. Sib. Fed. Univ. Engineer. Technol. 6 (4), 450–454.
Sánchez España, J., Pamo, E.L., Pastor, E.S., Andrés, J.R., Rubí, J.A.M., 2006. The impact of acid mine drainage on the water quality of the Odiel River (Huelva, Spain): evolution of precipitate mineralogy and aqueous geochemistry along the Concepción-Tintillo segment. Water Air Soil Pollut. 173 (1), 121–149. https://doi.org/10.1007/s11270-005-9033-6.
Sánchez-España, J., Yusta, I., Gray, J., Burgos, W.D., 2016a. Geochemistry of dissolved aluminum at low pH: extent and significance of Al–Fe(III) coprecipitation below pH 4.0. Geochim. Cosmochim. Acta 175, 128–149. https://doi.org/10.1016/j.gca.2015.10.035.
Sánchez-España, J., Yusta, I., Burgos, W.D., 2016b. Geochemistry of dissolved aluminum at low pH: hydrobasaluminite formation and interaction with trace metals, silica and microbial cells under anoxic conditions. Chem. Geol. 441, 124–137. https://doi.org/10.1016/j.chemgeo.2016.08.004.
Sani, R.K., Peyton, B.M., Brown, L.T., 2001. Copper-induced inhibition of growth of *Desulfovibrio desulfuricans* g20: assessment of its toxicity and correlation with those of zinc and lead. Appl. Environ. Microbiol. 67 (10), 4765–4772. https://doi.org/10.1128/AEM.67.10.4765-4772.2001.
Siew, Y.W., Zedda, K.L., Velizarov, S., 2020. Nanofiltration of simulated acid mine drainage: effect of ph and membrane charge. Appl. Sci. 10 (1), 400. https://doi.org/10.3390/app10010400.
Smith, K.S., 1999. Metal sorption on mineral surfaces: an overview with examples relating to mineral deposits. In: Plumlee, G.S., Losdon, M.J. (Eds.), The Environmental Geochemistry of Mineral Deposits, Part A. Processes, Techniques, and Health Issues. Society of Economic Geologists, Littleton, CO, pp. 161–182.
Song, Y., Liu, Y., Wang, H., 2018. Comparison of the biological and chemical synthesis of schwertmannite at a consistent $Fe^{2+}$ oxidation efficiency and the effect of extracellular polymeric substances of *Acidithiobacillus ferrooxidans* on biomineralization. Materials 11 (9), 1739. https://doi.org/10.3390/ma11091739.
Stookey, L.L., 1970. Ferrozine - a new spectrophotometric reagent for iron. Anal. Chem. 42 (7), 779–781. https://doi.org/10.1021/ac60289a016.
Velasco, E., Mason, P., Vroon, P., Röling, W., Amils, R., Davies, G., 2011. Microbial sulfur isotope fractionation in a Mars analogue environment at Rio Tinto, SW Spain. EPSC-DPS Joint Meeting 2011: Nantes, France vol. 6 , p. 460. http://meetings.copernicus.org/epsc-dps2011.
Wang, H., Gong, L., Cravotta, C.A., Yang, X., Tuovinen, O.H., Dong, H., Fu, X., 2013. Inhibition of bacterial oxidation of ferrous iron by lead nitrate in sulfate-rich systems. J. Hazard. Mater. 244-245, 718–725. https://doi.org/10.1016/j.jhazmat.2012.11.004.
Webb, S.M., 2005. SIXPack a graphical user interface for XAS analysis using IFEFFIT. Phys. Scr., 1011 https://doi.org/10.1238/physica.topical.115a01011.
Yilmaz, A., Yanar, A., Alkan, E., 2018. Review of heavy metal accumulation in aquatic environment of Northern East Mediterranean Sea part II: some non-essential metals. Pollut. 4 (1), 143–181. https://doi.org/10.22059/POLL.2017.236121.287.
Zhang, J., Zhou, F., Chen, C., Sun, X., Shi, Y., Zhao, H., Chen, F., 2018. Spatial distribution and correlation characteristics of heavy metals in the seawater, suspended particulate matter and sediments in Zhanjiang Bay, China. PLoS One 13 (8), e0201414. https://doi.org/10.1371/journal.pone.0201414.